ImplicitTerrain: a Continuous Surface Model for Terrain Data Analysis

Haoan Feng, Xin Xu, Leila De Floriani
University of Maryland, College Park
{hfengac, xinxu629, deflo}@umd.edu

ImplicitTerrain: a Continuous Surface Model for Terrain Data Analysis

Supplementary Material

Contents

1. Morse-based Topological Analysis on Terrain Data

1.1. Background

Simplical Complex a *k-simplex* σ is the convex hull of $k+1$ affinely independent points in the Euclidean space. A *simplicial complex* Σ is a finite set of simplexes, such that: (i) each face of a simplex in Σ belongs to Σ; (ii) for each pair of simplexes σ and τ, either $\sigma \cap \tau = \emptyset$ or $\sigma \cap \tau$ is a face of both. The *k-skeleton* of a d-dimensional complex Σ (with $k \leq d$) is the subset of containing the cells of Σ of dimension less than or equal to k.

Discrete Morse theory Forman theory [5] is a combinatorial counterpart of Morse theory which extends the results of Morse theory to discrete data. Given a simplicial complex Σ, a discrete vector is a pair of simplexes (σ, τ), where σ is a face of τ. A *discrete vector field* V is a collection of pairs (σ, τ) such that, each simplex of Σ is in at most one pair of V. Simplices that are not the tail or the head of a vector are called *critical*. In a triangle mesh, critical triangles are maxima, critical edges are saddles and critical vertices are minima. Pairs are formed by a triangle and an edge; and by an edge and a vertex. A *V-path* is a sequence $\sigma_1, \tau_1, \sigma_2, \tau_2, ..., \sigma_r, \tau_r$, such that $(\sigma_i, \tau_i) \in V$, σ_{i+1} is a face of τ_i, and $\sigma_i \neq \sigma_{i+1}$. A V-path with $r > 1$ is *closed* if σ_1 is a facet of τ_r different from σ_{r-1}. A discrete vector field V is called a *Forman gradient* if it has no closed V-paths. A *separatrix* V_i-path is a V-path connecting two critical simplexes of dimension $i+1$ and i, respectively. In a triangle mesh, we have each separatrix V_0-path connecting a critical edge to a critical vertex and separatrix V_1-path connecting a critical triangle to a critical edge. Critical simplices are the discrete counterpart of critical points and separatrix V-paths are the discrete counterpart of the integral lines in the continuous case. Any descending k-manifold, is the collection of the k-simplices of Σ reached by the gradient paths starting from a critical k-simplex. Dually, an ascending k-manifold is the collection of the $(d\text{-}k)$-simplices reached by the gradient paths (visited backward) starting from a critical $(d\text{-}k)$-simplex. The collection of the descending and ascending manifolds forms the discrete ascending and descending Morse complexes, respectively.

1.2. Morse Incidence Graph (MIG) simplification

We simplify a Morse Incidence Graph (MIG) to discard insignificant critical points that do not contribute to the main topological structure, thus focusing on preserving the most relevant topological features [2, 3].

To do so, we employ a persistence-based simplification approach on the MIG. Persistence measures the importance of a pair of connected critical points. In a MIG G, for each arc e connecting two critical points p_1 and p_2, the persistence value of e is calculated as $\min(|f(e)-f(p_1)|, |f(e)-f(p_2)|)$, where f is a scalar function defined on the input data (see Background Section in the manuscript).

Follow the critical point cancellation operation in [2], Algorithm 1 iteratively cancels the pairs of *Saddle-Maximum* or *Saddle-Minimum* with low persistence value and updates the MIG connectivity. The remaining nodes and arcs comprise the fundamental topological characteristics of G. Please note that critical points close to the boundary are removed to minimize boundary effects.

1.3. 1-Wasserstein distance for persistence diagrams

The Wasserstein distance quantifies the discrepancy between two probability measures. Sliced The Sliced Wasserstein distance [8] offers an approximation of this metric in 1D space. Sliced Wasserstein distance simplifies computation by considering one-dimensional projections of the distributions. Instead of calculating the distance directly in a high-dimensional space, the distributions are divided into multiple one-dimensional projections, and the 1-Wasserstein distances for these projections are computed and aggregated.

We applied sliced Wasserstein kernels introduced for persistence diagrams [1] with the implementation from Persim Package [1] to calculate the sliced Wasserstein distance.

[1] Publicly accessible at https://persim.scikit-tda.org/

Algorithm 1 Morse Incidence Graph simplification.

Require: $G(N, E)$: Morse Incidence Graph, $pthresh$: persistence threshold
N: Set of nodes with $n(index, v)$, where $index \in \{0 : \text{minimum}, 1 : \text{saddle}, 2 : \text{maximum}\}$ and v is the scalar function value.
E: Set of arcs with $e(s, m, v)$, where saddle s, non-saddle $m \in N$, and v is the persistence value.

Sort arcs E in ascending order of persistence values.
$e(m, s, v) \leftarrow G.E[0]$
while $e.v \leq pthresh$ **do**
  Remove nodes s and m from N.
  Remove arc e from E.
  for each neighbor p of s, if $p \neq m$ **do**
    for each neighbor q of m, if $q \neq s$ **do**
      Add arc $(p, q, |p.v - q.v|)$ to E.
      Re-sort E in ascending order of persistences.
      $e(m, s, v) \leftarrow G.E[0]$
      Break and return to the start of the WHILE loop.
    end for
  end for
end while

1.4. Influence of mesh configuration to discrete Forman method

For the *Forman method* applied to the regular gridded data, Delaunay trianglation [4]results vary a lot, because for each squared cell from the raster data, the diagonal connection between vertices is not determinant by the Delaunay triangulation. This difference in triangulation results, known as the *mesh configuration*, might lead to different topological analysis results for the same terrain data. For example, in Fig. 1 and Fig. 2, we plot a region influenced by the *mesh configuration* in the Swiss$_1$ dataset. We consider two *mesh configurations* for the *Forman method*: for each vertice, we connect it to its (N, S, E, W, NW, SE) neighbors or (N, S, E, W, NE, SW) neighbors, named as *Mesh1* and *Mesh2*, respectively. As illustrated in the yellow circled region in Fig. 1, the connectivity of the *Mesh2* appears to be more reasonable than the *Mesh1* in the region. The separatrix lines in the *Mesh2* are more aligned with the results from ImplicitTerrain which follows the gradient of the terrain surface. The *mesh configuration* in *Mesh1* seems to hinder the separatrix lines to move in the NE and SW directions, while in the meantime, encouraging the separatrix lines to move in the NW and SE directions. As a result, the MIGs obtained from the *Mesh1* and *Mesh2* are different, leading to Wasserstein distance between the two MIGs, as shown in Fig. 6 and Tab. 1. To accommodate this influence, we propose to use the ratio of Wasserstein distance as described in the main paper.

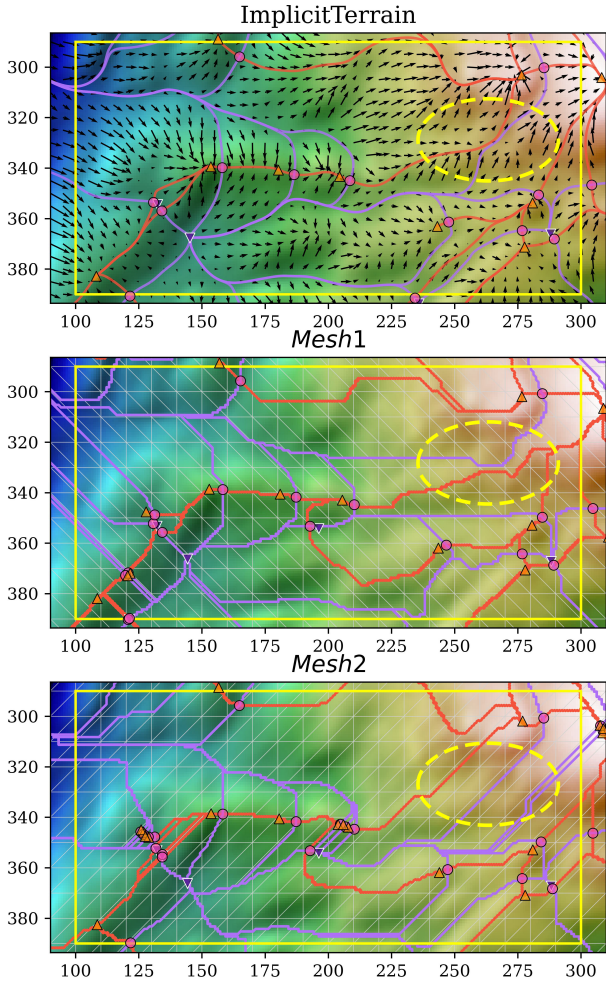

Figure 1. A zoomed-in region of the mesh configuration influence the topological analysis results. The yellow box is the zoomed-in region and the yellow circle denotes the main difference between the methods. In the first plot of ImplicitTerrain, we show the estimated gradient field by the pixel shifting method. In the two underlying plots, we use the light gray colored mesh to indicate the *mesh configuration* of *Mesh1* and *Mesh2*, respectively. Note it is a low-resolution illustration of the connection.

2. Tracing Gradient Field for Topological Analysis

According to Sylvester's criterion [6], critical point classification can be achieved by analyzing the second-order derivative (i.e. *Hessian* matrix $\mathcal{H} \in \mathbb{R}^2$) at the critical point coordinate $\vec{p}$ and it takes the form:

$$\mathcal{H}|_{\vec{p}} = \begin{bmatrix} \frac{\partial^2 \mathcal{F}_s}{\partial x^2} & \frac{\partial^2 \mathcal{F}_s}{\partial x \partial y} \\ \frac{\partial^2 \mathcal{F}_s}{\partial y \partial x} & \frac{\partial^2 \mathcal{F}_s}{\partial y^2} \end{bmatrix} = \begin{bmatrix} f_{xx} & f_{xy} \\ f_{yx} & f_{yy} \end{bmatrix} \quad (1)$$

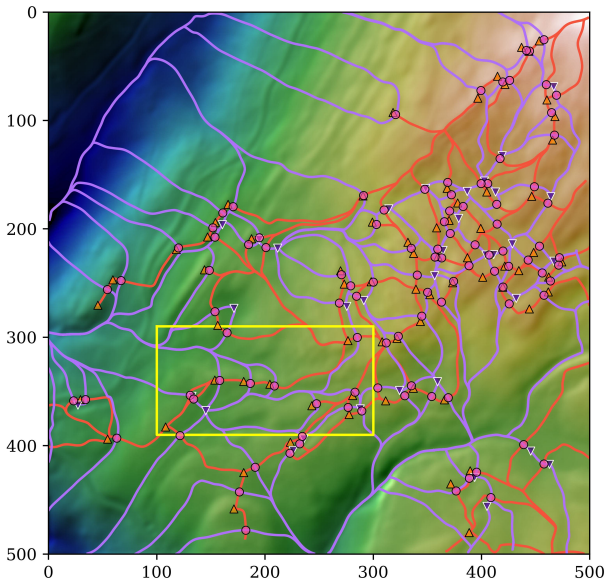

Figure 2. An overview of the mesh configuration influence on the topological analysis results. Yellow box indicates the zoomed-in region in Fig. 1.

$$\text{Type}(\vec{p}) = \begin{cases} Saddle & \text{if } \det(\mathcal{H}|_{\vec{p}}) < 0 \\ Maximum & \text{if } \det(\mathcal{H}|_{\vec{p}}) > 0 \text{ and } f_{xx} < 0 \\ Minimum & \text{if } \det(\mathcal{H}|_{\vec{p}}) > 0 \text{ and } f_{xx} > 0 \end{cases} \tag{2}$$

where $\mathcal{H}|_{\vec{p}}$ is the Hessian matrix at $\vec{p}$ and $\det(\mathcal{H}|_{\vec{p}})$ is its determinant. To locate the critical point, we trace the points whose gradient norm is zero. In practice, critical point candidate locations are pre-selected by comparing the difference between neighboring data points as in [9]. Clone and random jitter of the coordinates are applied to these candidate coordinates. Starting from these candidate points, a step-by-step gradient norm minimization (as in Algorithm 2) is applied to gradually move these points into locations with gradient norms less than a threshold (e.g. 1e-4). Converged locations are further classified into different types of critical points and used as input for the separatrix line tracing stage. To minimize the gradient norm $||\nabla\Psi_s||$, the gradient descent direction $\vec{d}$ is calculated as:

$$\begin{aligned} \vec{d} &= -\langle \partial||\nabla\Psi_s||/\partial x, \partial||\nabla\Psi_s||/\partial y\rangle \\ &= -\langle f_x f_{xx} + f_y f_{yx}, f_x f_{xy} + f_y f_{yy}\rangle \end{aligned} \tag{3}$$

where f_x, f_y are the first-order derivatives of Ψ_s and $f_{xx}, f_{xy}, f_{yx}, f_{yy}$ are the second-order derivatives.

After identification of critical points, we apply a numerical tracing algorithm (as in Algorithm 3) to trace the separatrix lines connecting critical points. The separatrix line is traced by following the maximum function increasing and decreasing directions from the critical point to the next critical point. The tracing is terminated when the gradient norm is below a threshold (e.g. 1e-4) or the tracing path reaches the boundary of the terrain data. The starting direction from each saddle point is discribed as in the main paper. The separatrix lines are used to construct the Morse Incidence Graph (MIG) for topological analysis.

Algorithm 2 Gradient Norm Minimization

Require: pts: candidate points
Require: $step\_size$: gradient descent step size
Require: Ψ: INR model
// By automatic differentiation
Function $gradient(\Psi, \vec{x})\{\cdots\}$
Function $Hessian(\Psi, \vec{x})\{\cdots\}$

Function grad_norm_minimization($pts, step\_size, \Psi$)
$converged\_pts \leftarrow [\,]$
// for–loop parallelized on GPU
while TRUE **do**
  for $\vec{p}$ in pts **do**
    $grad\_norm \leftarrow norm(gradient(\Psi, \vec{p}))$
    if $grad\_norm < .0001$ **then**
      $converged\_pts.add(\vec{p})$
      remove $\vec{p}$ from pts
      if pts is empty **then**
        break
      end if
    end if
    $\mathcal{H} \leftarrow Hessian(\Psi, \vec{p})$
    $f_{xx}, f_{xy}, f_{yx}, f_{yy} \leftarrow \mathcal{H}$
    $\vec{d} \leftarrow -\langle f_x f_{xx} + f_y f_{yx}, f_x f_{xy} + f_y f_{yy}\rangle$
    $\vec{p} \leftarrow \vec{p} + step\_size \cdot \vec{d}$
    // Update step size for next iteration if needed
  end for
end while
return $converged\_pts$
EndFunction

In our tracing algorithms, we avoid identifying the critical points on the boundary of the terrain data, as they are not reliable as topological features of the tile. Different methods may handle the boundary differently during the identification of critical points and construction of the MIG. Therefore, to avoid the influence of the boundary, we only consider the critical points inside the terrain data for the topological analysis and also filtered out the critical points on the boundary for results from the *Forman method*. Separatrix lines that reach the boundary are also discarded during the MIG construct stage.

Algorithm 3 Trace Separatrix Lines from Saddle points

Require: pts: *Saddle* points
Require: $step\_size$: gradient descent step size
Require: Ψ: INR model
// Eigen decomposition return sorted eigenvalues and eigenvectors
Function $eigen(\mathcal{H})\{\cdots\}$

Function separatrix_lines($pts, step\_size, \Psi$)
// for–loop parallelized on GPU
for $\vec{p}$ in pts **do**
$\vec{p_1} = \vec{p_2} = \vec{p_3} = \vec{p_4} \leftarrow \vec{p}$
// replace $\vec{p}$ with $\vec{p_i}$ in the pts
$\lambda_1, \lambda_2, \vec{v_1}, \vec{v_2} \leftarrow eigen(Hessian(\Psi, \vec{p}))$
$sign_1 = sign_2 \leftarrow 1$
$sign_3 = sign_4 \leftarrow -1$
for i in $1, 2, 3, 4$ **do**
$pathes[i] \leftarrow [\,]$
$\vec{p_i} \leftarrow \vec{p_i} + sign_i \cdot step\_size \cdot \vec{d}$
end for
for i in $1, 2, 3, 4$ **do**
while TRUE **do**
$pathes[i].add(\vec{p_i})$
$\vec{d} \leftarrow gradient(\Psi, \vec{p_i})$
$grad\_norm \leftarrow norm(\vec{d})$
if $grad\_norm < .0001$ **then**
remove $\vec{p_i}$ from pts
if pts is empty **then**
break
end if
end if
$\vec{p_i} \leftarrow \vec{p_i} + sign_i \cdot step\_size \cdot \vec{d}$
end while
end for
end for
return $pathes$
EndFunction

3. Experiment Results for Swisstopo Datasets

For the four tiles of Swisstopo datasets we used in the paper, we provide the detailed experiment results in terms of the fitting, topological, and topographical analysis. For each tile in the swissALTI3D [10] dataset, its tile name can be uniquely identified by the tile's row and column coordinate in the dataset. The tile name of Swiss_1 is 2494_1141, Swiss_2 is 2717_1187, Swiss_3 is 2710_1195, and Swiss_4 is 2641_1180. These four tiles are selected to represent different terrain characteristics as shown in Fig. 3.

3.1. Fitting Results

Numerical results are reported in the main paper, while we provide more visualizations of the terrain tiles and our reconstructed results in this section. As shown in Fig. 3, we provide the original terrain data, the reconstructed data by ImplicitTerrain, the displacement map used for *Geometry model* fitting, and the gradient field visualization. Note the existence of cliffs in the Swiss_2 and Swiss_3 datasets, which are challenging for the fitting process. The gradient field visualization shows that at the cliff regions, the gradient magnitude is much larger than in other regions, which poses a challenge for the fitting process. However, the gradient angle difference is small. According to the gradient field tracing algorithms we used in this paper, as long as the gradient angle is correct and consistent, the topological analysis results should be reliable. This is also confirmed by the topological analysis results for the four tiles. Even though different tiles have different terrain characteristics, our pipeline is flexible and powerful enough to handle them with the same pipeline configuration. In Fig. 4, we provide the analysis of difference maps between the smoothed terrain data and the *Surface model* estimation by ImplicitTerrain. For each dataset, we show the pixel-wise absolute difference map, the Fourier spectrum of the smoothed data, the Fourier spectrum of the model estimation, and the difference between the two spectra. From our observation, there is no direct relationship between the PSRN value and the frequency domain difference. Since PSNR is related to the average loss of the fitting result, good fitting of low-frequency components of the terrain data might lead to a high PSNR value. Also for topological analysis, the low-frequency components contribute more to the overall shape of the terrain surface, which means a good fitting of low-frequency components will benefit the accuracy of topological analysis. However, the high-frequency components are also important for the visual quality of the reconstruction, as the high-frequency components are related to the detailed terrain features. Note that different tiles have different frequency components, in future work, we think this difference can be used to guide the network configurations for different terrain tiles.

We plot the gradient magnitude estimated by the image pixel shifting method and our *Surface model* in Fig. 5. The gradient magnitude difference (GMD) and gradient angle difference (GAD) are calculated between the two gradient fields. The GMD and GAD are all in the normalized range $[-1, 1]$ of the input so that all the tiles can be plotted in the same color coding. Larger differences in the gradient magnitude happen in the regions with large gradient change, or in other words, with more complex topology, *e.g.*, cliff regions. This is because fitting such drastic changes might already exceed the capability of current network configurations, and also because the estimation from the image pixel

shifting method may not be accurate in these regions. As discussed in the fitting results, the gradient angle difference is small, which is a good sign for the topological analysis. Moreover, apart from the drastic changing regions, larger GAD values are also observed in the regions with much smaller gradient magnitudes, which are likely to be flat regions. For topological analysis, flat regions usually do not contain critical points and rarely contribute to the terrain surface's topological features [11]. Therefore, the gradient angle difference in these regions is not a big concern for our topological analysis.

3.2. Topological Analysis Results

Apart from Tab. 1, we provide the visualization of the topological features extracted from the four tiles in Figs. 6 to 9. For each dataset, we show the critical points, the separatrix lines, and the Morse Inequalities Graph (MIG) obtained from the *Forman method*. Results from both *Mesh1* and *Mesh2* are shown together with the results from ImplicitTerrain. In the last column of each figure, we plot the persistence diagrams from the corresponding MIGs. The persistence diagram from ImplicitTerrain is overlaid with the persistence diagram from *Mesh1* and *Mesh2* for comparison.

3.3. Topographical Analysis Results

Topographical features can be obtained from the surface derivatives estimated by the *surface model*. As mentioned in the main paper, the normal direction of the terrain surface can be obtained as $\langle -f_x, -f_y, 1\rangle$, where f_x and f_y denote the first order derivative of the surface function in x and y directions. In Fig. 10, we plot the *Normal mapping* to visualize the normal direction of the terrain surface, in which the (x, y, z) normal direction is color encoded as (r, g, b) channels, correspondingly. The *slope* and *aspect* are calculated from the normal direction, where the slope is the angle between the normal direction and the vertical direction, and the aspect is the angle between the normal direction and the north direction.

With the capability to obtain the second-order derivatives, the curvature of the terrain surface can also be calculated. According to [7], the mean curvature of the manifold takes the form:

$$H = \frac{(1+f_y^2)f_{xx} - 2f_x f_y f_{xy} + (1+f_x^2)f_{yy}}{2(1+f_x^2+f_y^2)^{3/2}} \quad (4)$$

where f_{xx}, f_{xy}, f_{yy} are the second-order derivatives of the function. In Fig. 10, we show the mean curvature of the terrain surface. The mean curvature is color encoded in the range of $[-0.5, 0.5]$, where the negative values represent the concave regions and the positive values represent the convex regions. From this curvature plot, we can also observe the different terrain characteristics of the four tiles.

References

[1] Mathieu Carriere, Marco Cuturi, and Steve Oudot. Sliced wasserstein kernel for persistence diagrams. In *International conference on machine learning*, pages 664–673. PMLR, 2017. 1

[2] Lidija Čomić, Leila De Floriani, Paola Magillo, and Federico Iuricich. *Morphological modeling of terrains and volume data*. Springer, 2014. 1

[3] Leila De Floriani, Ulderico Fugacci, Federico Iuricich, and Paola Magillo. Morse complexes for shape segmentation and homological analysis: discrete models and algorithms. In *Computer graphics forum*, pages 761–785. Wiley Online Library, 2015. 1

[4] Boris Delaunay et al. Sur la sphere vide. *Izv. Akad. Nauk SSSR, Otdelenie Matematicheskii i Estestvennyka Nauk*, 7 (793-800):1–2, 1934. 2

[5] Robin Forman. Morse theory for cell complexes. *Advances in mathematics*, 134(1):90–145, 1998. 1

[6] George T Gilbert. Positive definite matrices and sylvester's criterion. *The American Mathematical Monthly*, 98(1):44–46, 1991. 2

[7] Barrett O'neill. *Elementary differential geometry*. Elsevier, 2006. 5

[8] Julien Rabin, Gabriel Peyré, Julie Delon, and Marc Bernot. Wasserstein barycenter and its application to texture mixing. In *Scale Space and Variational Methods in Computer Vision: Third International Conference, SSVM 2011, Ein-Gedi, Israel, May 29–June 2, 2011, Revised Selected Papers 3*, pages 435–446. Springer, 2012. 1

[9] Luigi Rocca, Bernhard Jenny, and Enrico Puppo. A continuous scale-space method for the automated placement of spot heights on maps. *Computers & Geosciences*, 109:216–227, 2017. 3

[10] Swisstopo. Swissalti3d datasets. https://www.swisstopo.admin.ch/en/height-model-swissalti3d, 2023. 4

[11] Kenneth Weiss, Federico Iuricich, Riccardo Fellegara, and Leila De Floriani. A primal/dual representation for discrete morse complexes on tetrahedral meshes. In *Computer Graphics Forum*, pages 361–370. Wiley Online Library, 2013. 5

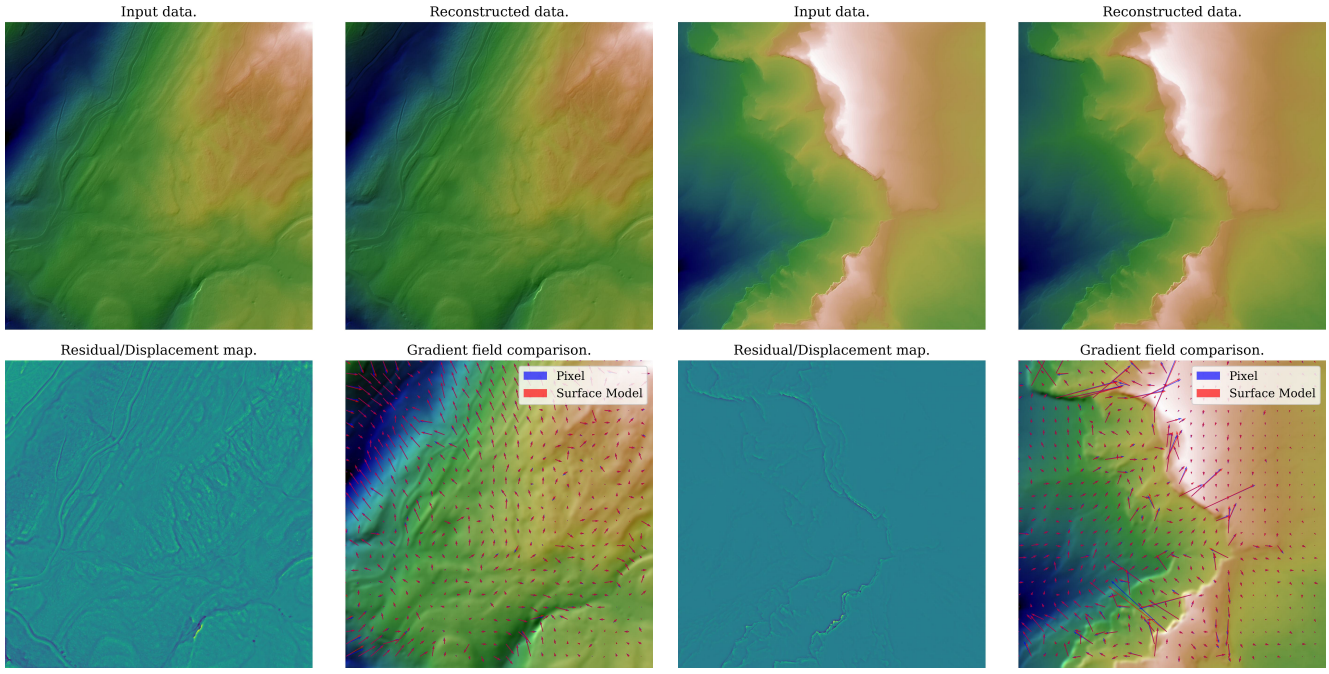

(a) Swiss$_1$ (b) Swiss$_2$

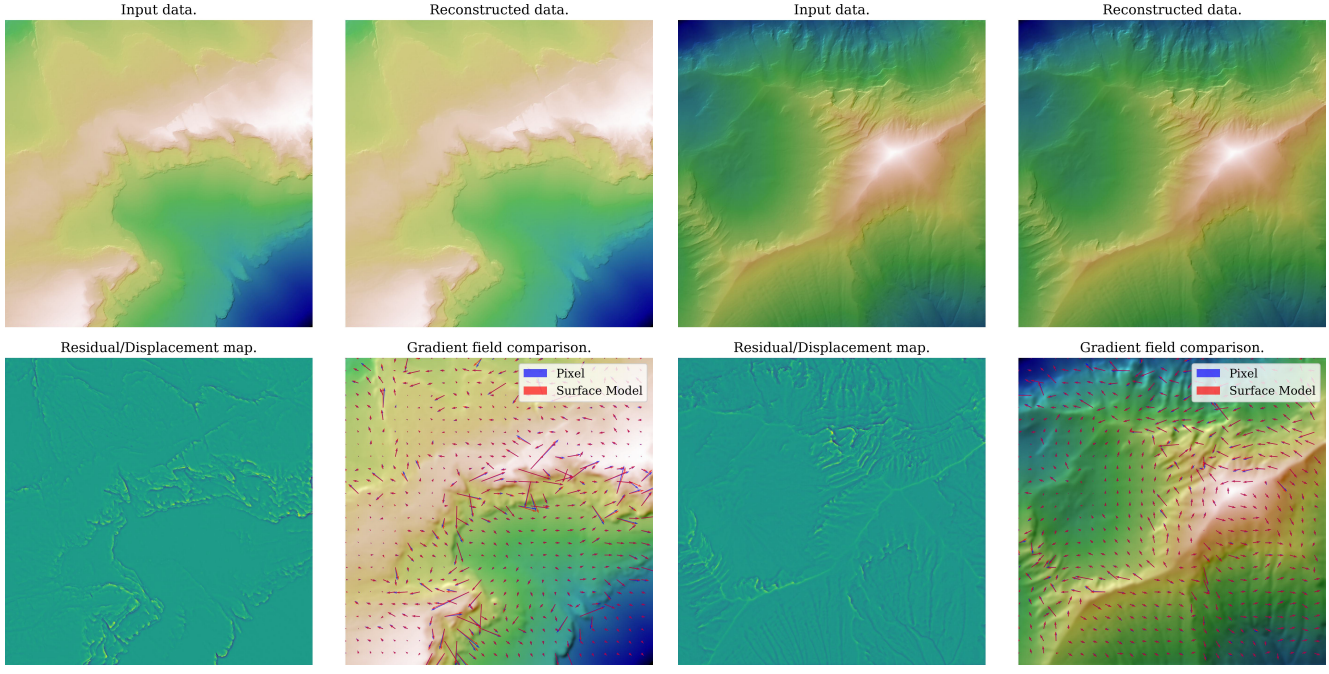

(c) Swiss$_3$ (d) Swiss$_4$

Figure 3. Fitting results for the four Swisstopo datasets. For each dataset, we show the original terrain data, the reconstructed data by ImplicitTerrain, the displacement map used for *Geometry model* fitting, and the gradient field visualization. For the gradient field, the red and blue colors represent the estimations by *Surface model* and image pixel shifting, respectively.

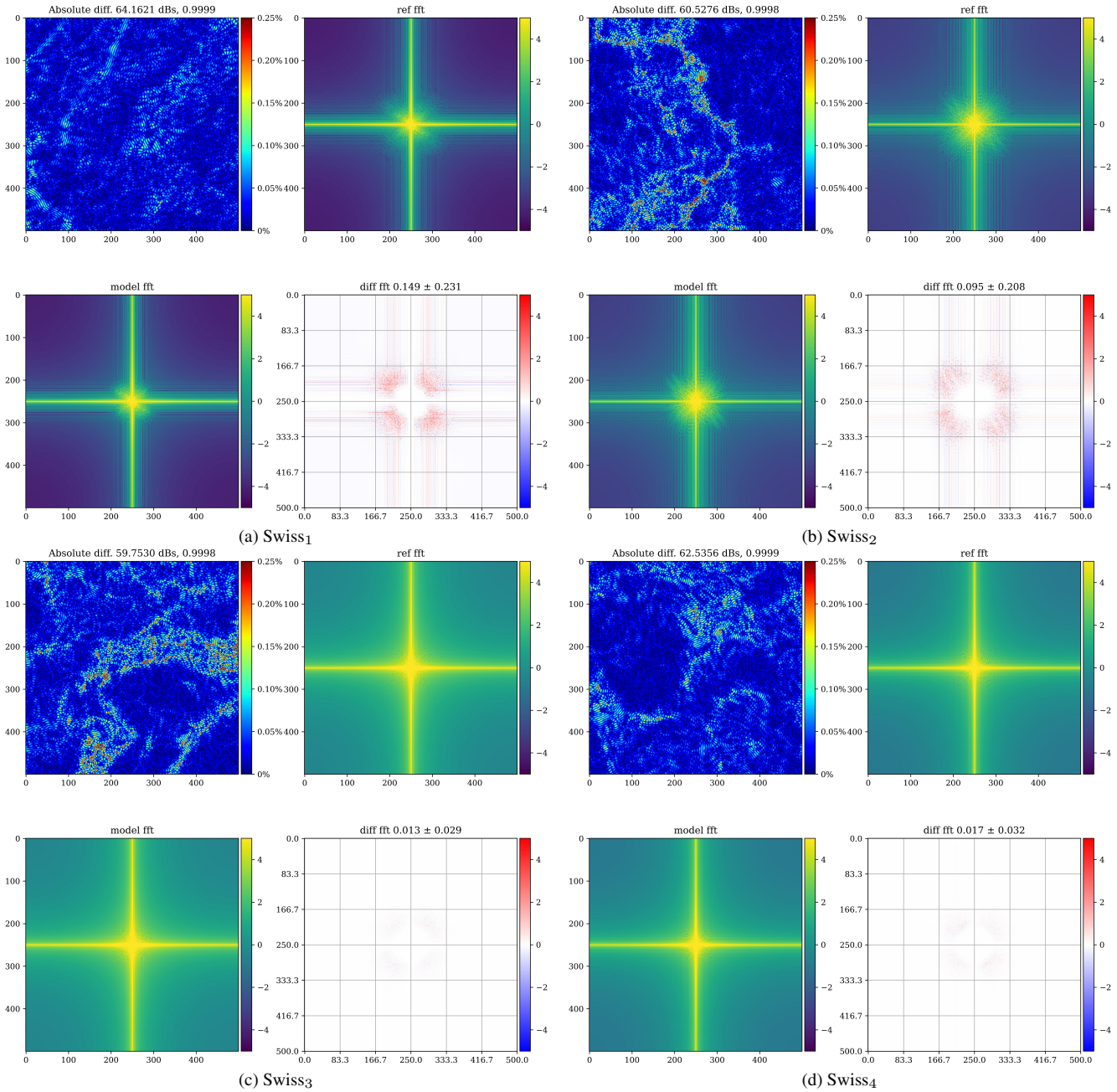

(a) Swiss$_1$ (b) Swiss$_2$

(c) Swiss$_3$ (d) Swiss$_4$

Figure 4. Analysis of difference maps between the smoothed terrain data and the *Surface model* estimation by ImplicitTerrain. For each dataset, we show the pixel-wise absolute difference map, the Fourier spectrum of the smoothed data, the Fourier spectrum of the model estimation, and the difference between the two spectra. Difference maps are color encoded with a cap to **0.25%** of the overall data range and PSNR and SSIM metrics are also displayed. For spectrum plots, the magnitude of the Fourier transform is shown in log scale within the range of $[10^{-5}, 10^{5}]$.

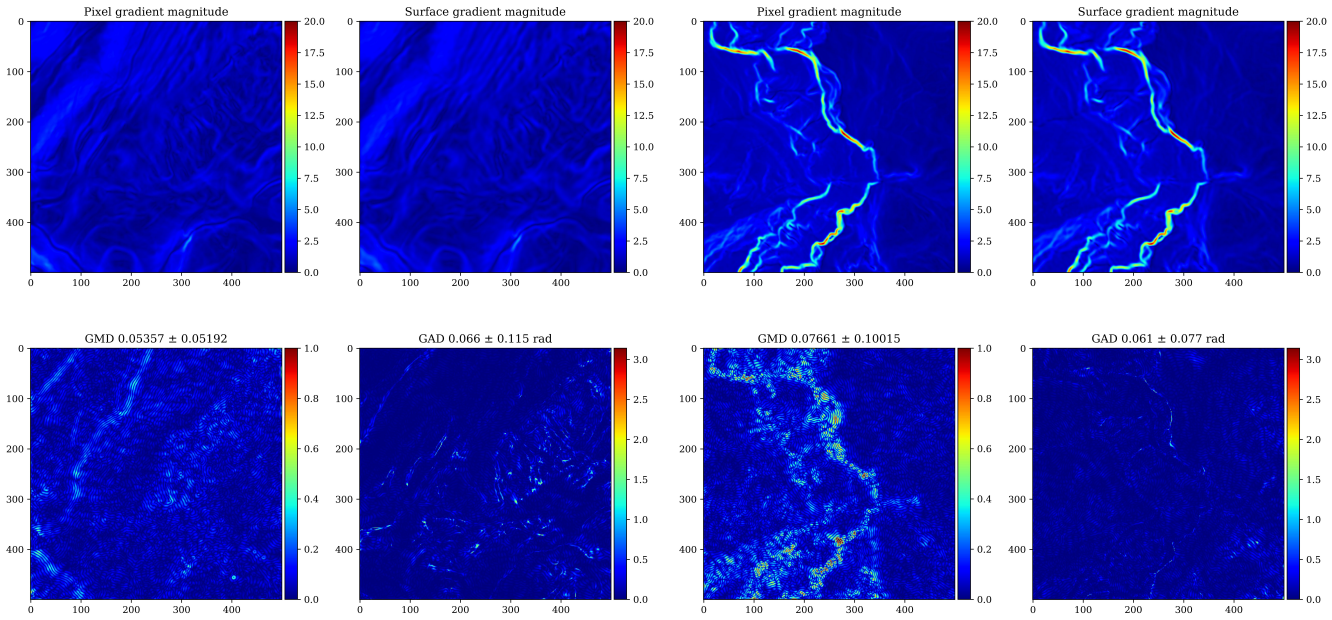

(a) Swiss$_1$

(b) Swiss$_2$

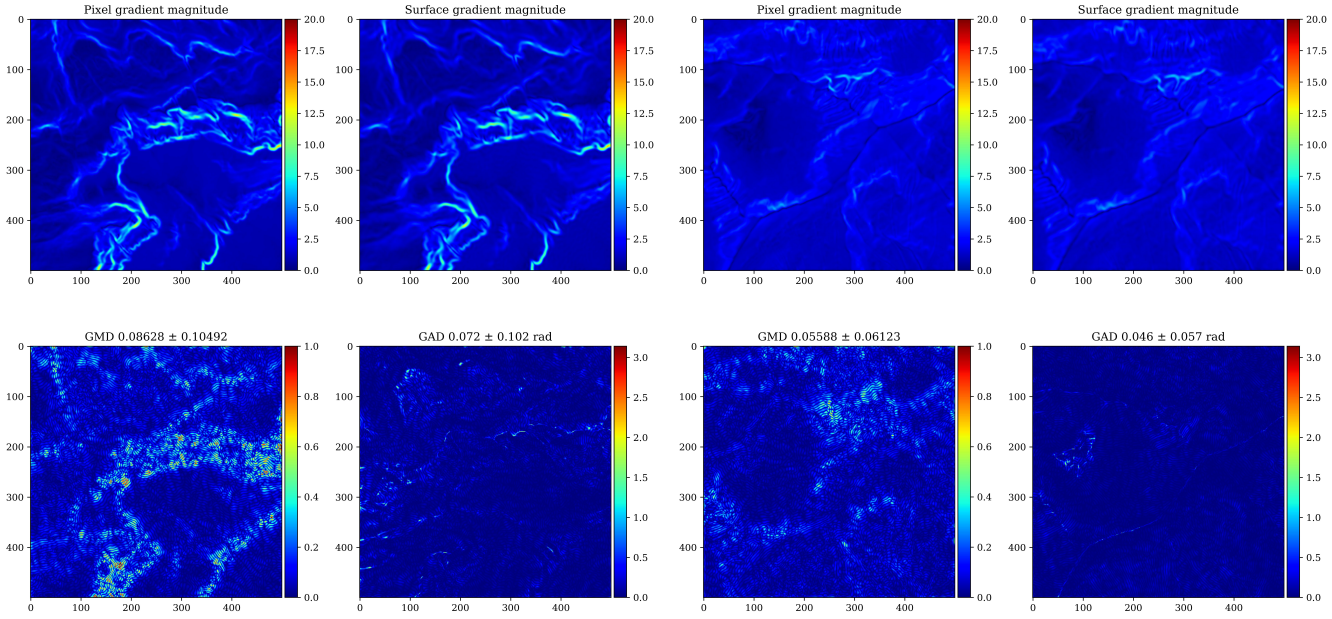

(c) Swiss$_3$

(d) Swiss$_4$

Figure 5. Analysis of gradient fields for the four Swisstopo datasets. For each dataset, we show the gradient field estimated by the gradient field estimated by pixel shifting on the smoothed terrain data and by the *Surface model*. The differences between the two gradient fields are displayed in gradient magnitude difference (GMD) and gradient angle difference (GAD). Both GMD and GAD's mean and standard deviation are reported in meters and radians, respectively.

Name	**precision**	**recall**	$F_{0.5}$ **score**	$WS(\Psi_s, Mesh1)$	$WS(\Psi_s, Mesh2)$	$WS(Mesh1, Mesh2)$	WS_{ratio}
Swiss$_1$	0.90	0.96	0.91	71.27	11.15	67.53	0.17
Swiss$_2$	0.91	0.831	0.89	86.65	24.19	78.65	0.31
Swiss$_3$	0.89	0.78	0.87	186.91	124.61	180.04	0.69
Swiss$_4$	0.91	0.83	0.89	47.86	171.68	137.92	0.35

Table 1. Topological analysis results of the Swisstopo datasets. WS denotes the Wasserstein distance between two persistence diagrams.

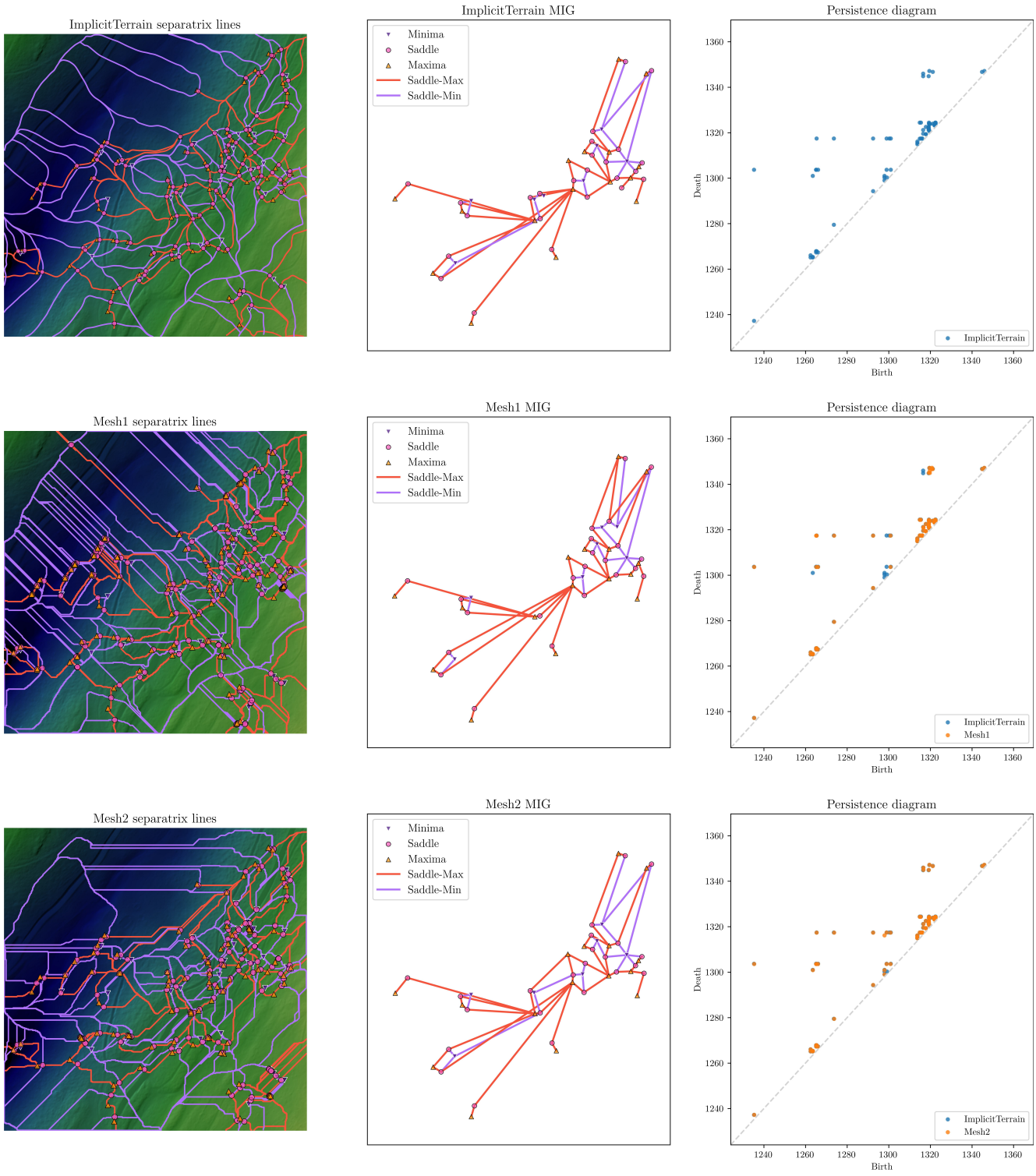

Figure 6. Topological analysis results of Swiss_1.

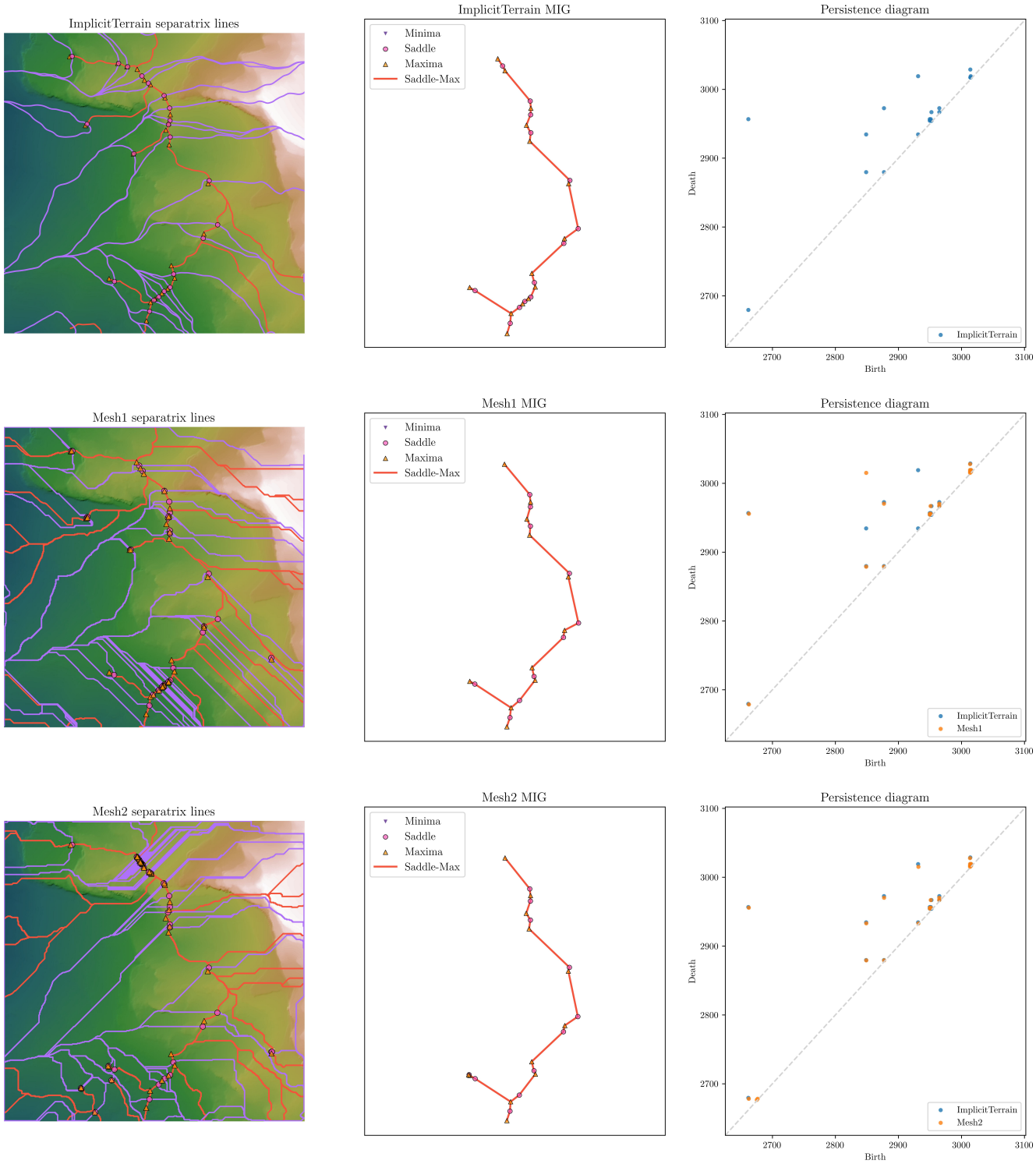

Figure 7. Topological analysis results of Swiss_2.

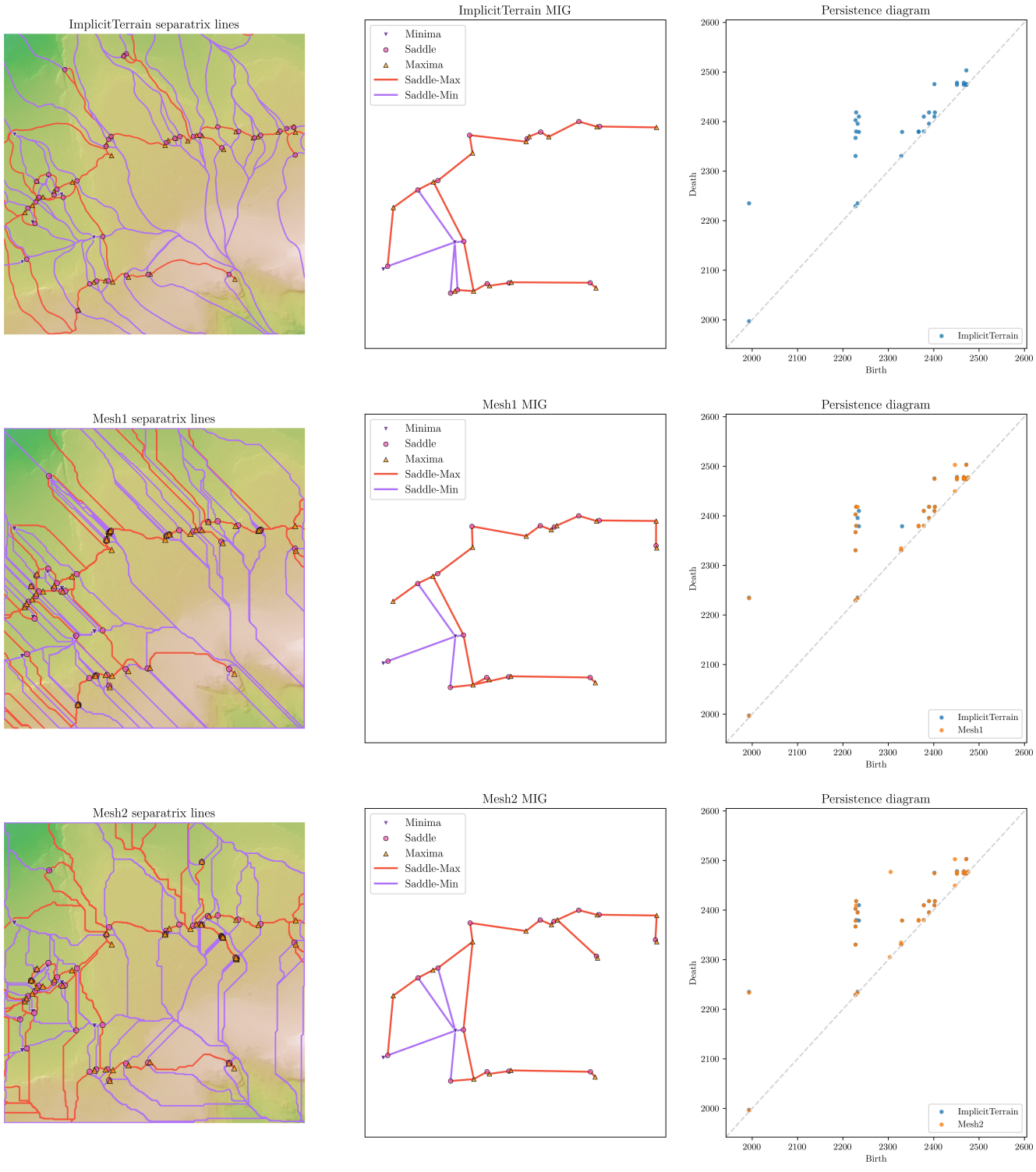

Figure 8. Topological analysis results of Swiss_3.

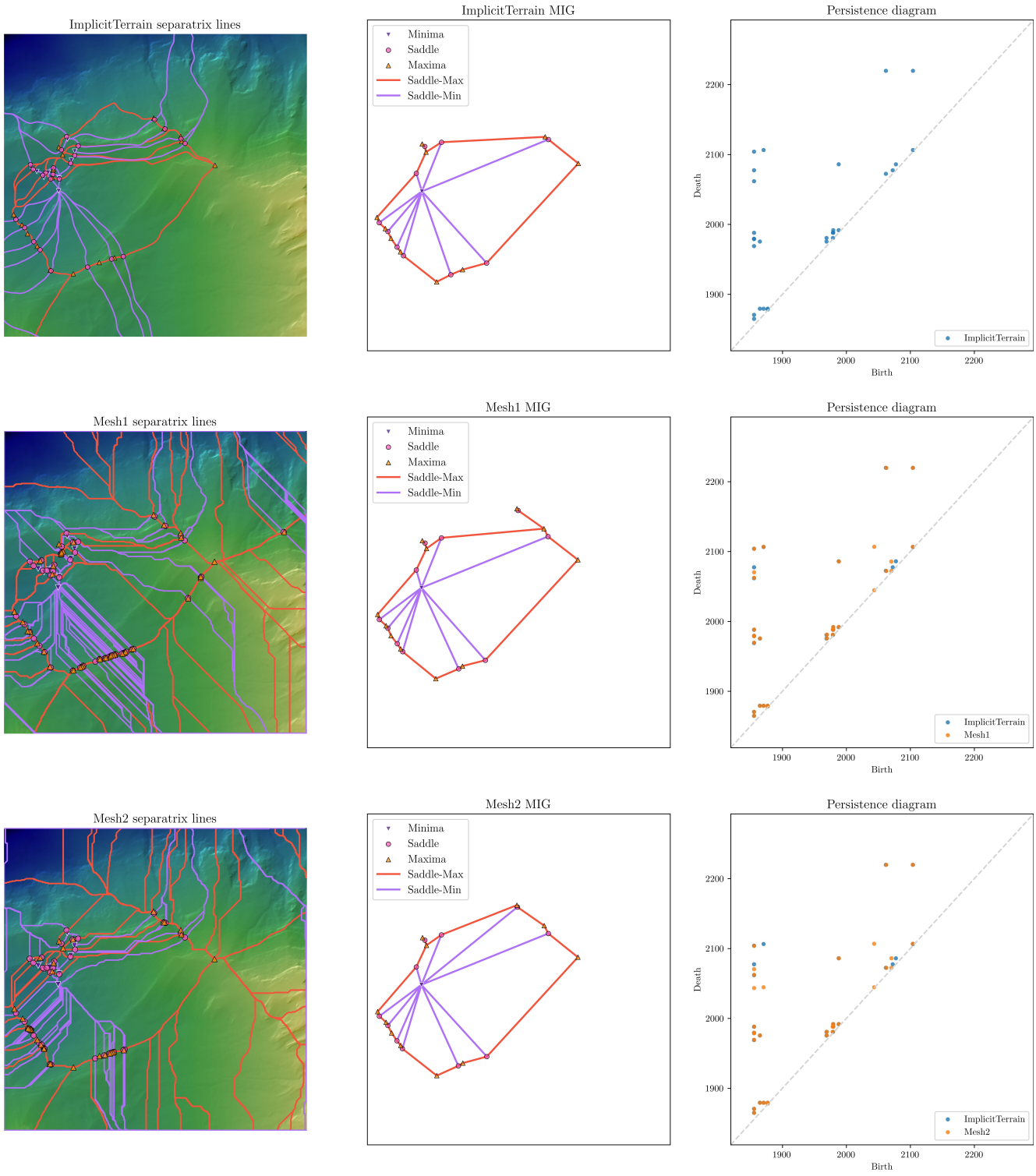

Figure 9. Topological analysis results of Swiss_4.

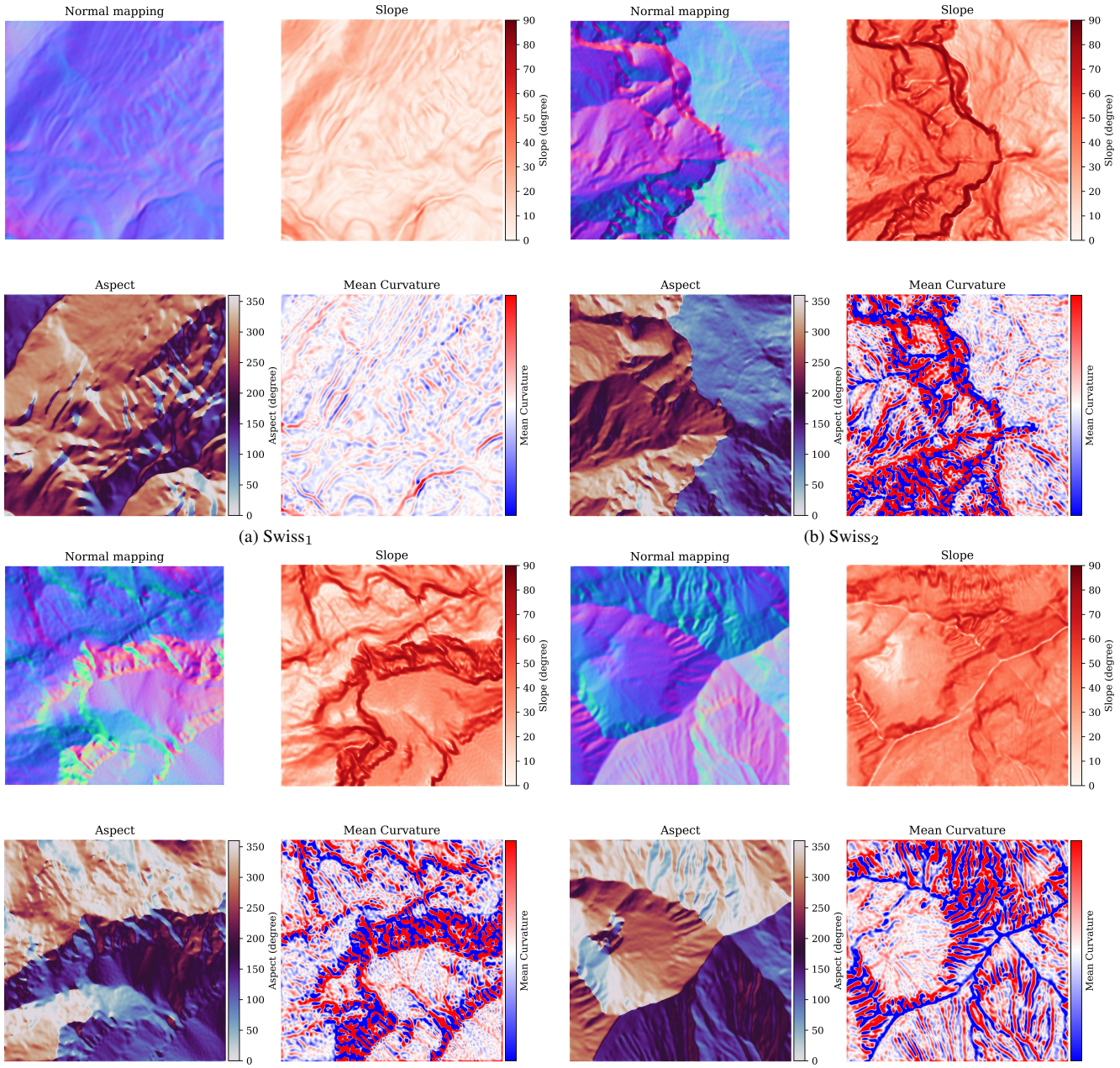

(a) Swiss$_1$ (b) Swiss$_2$

(c) Swiss$_3$ (d) Swiss$_4$

Figure 10. Topographical analysis results for the four Swisstopo datasets. For each dataset, we show the normal mapping, slope, aspect, and mean curvature of the terrain surface estimated by the ImplicitTerrain. For slope and aspect, values are in degrees. For mean curvature, values are in meters^{-1} and color encoded in the range of $[-0.5, 0.5]$.